big data and cognitive computing

MDPI

Article

Machine Learning-Based Prediction of Operability for Friction Pendulum Isolators Under Seismic Design Levels

Ayla Ocak [1], Batuhan Kahvecioğlu [1], Sinan Melih Nigdeli [1], Gebrail Bekdaş [1,*], Ümit Işıkdağ [2] and Zong Woo Geem [3,*]

[1] Department of Civil Engineering, İstanbul University-Cerrahpaşa, 34320 İstanbul, Türkiye; aylaocak@outlook.com (A.O.); batuhankahvecioglu@gmail.com (B.K.); melihnig@iuc.edu.tr (S.M.N.)
[2] Department of Architecture, Mimar Sinan Fine Arts University, 34427 İstanbul, Türkiye; umit.isikdag@msgsu.edu.tr
[3] College of IT Convergence, Gachon University, Seongnam 13120, Republic of Korea
* Correspondence: bekdas@iuc.edu.tr (G.B.); geem@gachon.ac.kr (Z.W.G.)

Abstract

Within the scope of the study, the parameters of friction pendulum-type (FPS) isolators used or planned to be used in different projects were evaluated specifically for the project and its location. The evaluations were conducted within a performance-based seismic design framework using displacement, re-centering, and force-based operability criteria, as implemented through the Türkiye Building Earthquake Code (TBDY) 2018. The friction coefficient and radius of curvature were evaluated, along with the lower and upper limit specifications determined according to TBDY 2018. The planned control points were the period of the isolator system, the isolator re-centering control, and the ratio of the base shear force to the structure weight. Within the scope of the study, isolator groups with different axial load values and different spectra were evaluated. A dataset was prepared by using the parameters obtained from the re-centering, period, and shear force analyses to determine the conditions in which the isolator continued to operate and those in which conditions prevented its operation. Machine learning models were developed to identify FPS isolator configurations that do not satisfy the code-based operability criteria, based on isolator properties, spectral acceleration coefficients corresponding to different earthquake levels, mean dead and live loads, and the number of isolators. The resulting Bagging model predicted an isolator's operability with a high degree of accuracy, reaching 96%.

Keywords: friction pendulum type isolator; machine learning; friction coefficient; radius of curvature

Check for updates

Academic Editor: Jiaming Li

Received: 6 November 2025
Revised: 30 December 2025
Accepted: 7 January 2026
Published: 12 January 2026

Copyright: © 2026 by the authors. Licensee MDPI, Basel, Switzerland. This article is an open access article distributed under the terms and conditions of the Creative Commons Attribution (CC BY) license.

1. Introduction

One of the most challenging external factors that needs to be overcome during the design phase in civil engineering is the effect of earthquakes. Many solutions have been developed over time to overcome this seismic effect. These solutions sometimes involve making the structure more resistant to earthquakes and sometimes involve reducing the seismic effect. The most effective method developed to reduce and absorb seismic effects is seismic isolation systems. The products used in seismic isolation systems are called isolators. Isolators are preferred in the superstructure in some cases and used in the substructure in others.

The base isolators used in the substructure are basically divided into two types. The systems used in the infrastructure vary depending on the materials and mechanisms.

Material-based isolators include natural, lead-core, or high-damping rubber-based isolators, while mechanism-based isolators are steel-based isolators. One of the most common steel-based isolators is the friction pendulum-type isolator (FPS) [1]. The main objectives of FPS-type isolators are to increase the structure's period and reduce the acceleration and torsional effects acting on the structure by utilizing the movement of the friction element coated according to its friction properties on the friction surface between the lower and upper steel plates. Another purpose is to provide additional damping to the structure by shifting the friction surface required by the structure during an earthquake. Considering the seismicity of the area, the design spectral acceleration is obtained, and the most appropriate friction–displacement relationship for the area is established using the friction properties of the FPS isolators for control. The friction properties of the FPS devices are essential for damping earthquake effects at the isolation level. The fundamental parameters for providing the basic friction properties required for structural vibration control are the friction coefficient and the radius of curvature of the FPS devices. These two parameters are known to influence structural displacement and acceleration. Seismic vibrations transmitted to the structure, particularly in earthquakes known for their destructive effects such as near-fault earthquakes, can cause large displacements at the isolator level, which can result in damage to the isolator. The differences in structural response caused by possible changes in the friction bearing have led to the development of variations in FPS devices with multiple sliding bearings [2–6], variable friction [7–12], and variable curvatures [13–19]. Jangid [20] observed that an increase in the friction coefficient in a structure equipped with an FPS under the influence of a near-fault was effective in reducing the structure's displacement, and he determined the optimum friction coefficient required to minimize the accumulated acceleration in the structure. Yin et al. [21] optimized the design parameters of friction pendulum isolators using a genetic algorithm that stands out with its convergence ability and determined the optimum value for the friction coefficient as 0.01 and the optimum value for the radius of curvature as 3.3 m. Sharma and Jangid [22] observed that a structure isolated with a variable frequency pendulum isolator and variable curvature friction pendulum system under near-field earthquakes caused a large displacement of the isolator when the initial radius of the curvature was high, and when the friction coefficient was increased, the displacement decreased; moreover, not being able to benefit from the benefits of the variable curvature and structural response was weakened. Duan [23] stated that, in the structure inter-story isolation system, the FPS slideway radius does not have a significant effect on the consumption of energy obtained by friction, and a certain increase in the friction coefficient is effective in reducing energy consumption. Fu et al. [24] reported that a structure isolated from the base by the rolling friction pendulum system was subject to a whipping effect when the friction of the FPS slideway was passing from low to high area in the variable friction case and suggested using low and constant friction isolation bearings instead of variable friction ones. Zhang et al. [25] proposed a concrete-filled steel pipe friction pendulum bearing system and observed that the elastic vertical bearing capacity could be improved by slightly increasing the radius of the spherical curvature surface. Zhuang et al. [26] used friction pendulum bearings (FPBs) in the seismic isolation of shell structures and stated that, by changing the FPB parameters, the increase in the radius of the curvature had a small effect on the structural response, while the increase in the friction coefficient had a significant effect on the seismic response.

FPS devices have become a widely used technique in the seismic isolation of buildings, bridges, and industrial structures due to their stability and durability compared to elastomeric isolators [27]. The actual seismic behavior of friction isolators is rarely verified, and the effect of velocity and temperature increases on the maximum displacement is uncertain [28]. While the effect of speed increase can be neglected, the effect of tempera-

ture increase on displacement is stated to be significant, especially in strong earthquakes and under the effects of near-faults [28]. Another feature that affects displacement is the period and re-centering properties of FPS isolators. The period of an isolator refers to the oscillation time of a tour required to dissipate energy in the isolation layer, while re-centering refers to the mechanism by which the isolator returns to its original position after movement to prevent permanent displacement. Failure to re-center the isolator can lead to permanent damage or failure to effectively perform its functions. In research conducted on this topic, a system was proposed to increase the seismic resistance and re-centering capability in isolated inter-story structures, and it was determined that the innovative system significantly impacted the seismic response [29]. In a proposed study on the triple friction pendulum system, the upper and lower sliding surfaces are designed with a small radius and a spherical geometry for the re-centering capability [30]. Isolator systems aim to extend the period of the structure. In doing so, the aim is to dissipate energy as much as possible without rupture at the isolator level and to minimize the shear force transferred to the superstructure. In a study conducted on the seismic protection of steel frame buildings with friction pendulum bearings (FPBs), it was observed that the case where the base shear force was the lowest was the case where the isolation period and yield strength ratio were the highest [31]. In the design of friction pendulum systems, careful consideration of friction properties, radius of the curvature, re-centering, superstructure forces, and the isolator period is essential for isolation efficiency. Furthermore, spectral acceleration values, depending on the seismicity of the region, are crucial in the design of FPS devices.

The regulations applicable to the region where the isolated structure is located serve as guidelines for the designs. The necessary design criteria for the FPS isolators discussed in this article have been calculated based on Turkish regulations. The rules applied to FPS isolators in Türkiye are defined in the 2018 Turkish Building Earthquake Code (TBEC2018) [32]. Çakat and Alemdar [33] applied modal and seismic analyses according to TBEC2018 on a 3D model of a hospital using FPS isolators and found that, while the fixed-base structure could not even meet the "Life Safety" performance level in maximum story drift, the FPS-equipped building met the "Immediate Occupancy" condition. Kaatsız et al. [34] examined the maximum and permanent displacements of five hospitals with FPS isolators located within 50 km of the region following two earthquakes (∼Mwg 7.7 and Mwg 7.5 [35]) that occurred in Türkiye on 6 February 2023 and observed that the post-earthquake displacements measured were lower than the design displacements and that the hospitals' structural systems did not sustain any damage. The studies conducted demonstrate that FPS isolators designed in accordance with regulations effectively fulfill their function in providing seismic protection for the structure.

Artificial intelligence prediction methods in the design of isolated structures stand out for their advantages in terms of calculation load and cost savings. In recent years, researchers have frequently used artificial intelligence techniques in their studies on seismic isolated structures. Studies have been conducted on the failure probability prediction of isolated structures [36], automating air bubble ratios in base plate concrete [37], isolation system design [38], seismic response prediction [39–41], maximum displacement prediction [42], pressure and shear parameter prediction [43], rubber bearing aging prediction [44], axial load prediction [45], and damping ratio prediction [46] using AI in seismic isolation. Artificial intelligence studies on FPS isolators, which are the subject of this article, have spread, especially in the last five years. It has been reported that the QFP properties can be predicted with a mean absolute percentage error value, with a maximum value below 5%, using a neural network model developed for the preliminary design of quintuple friction pendulum (QFP) isolators [47]. It has been found that the nonlinear hysteresis behavior of triple pendulum bearing isolators can be well predicted by

the recurrent neural network model [48]. An AI-assisted analytical method using artificial intelligence (AI) was proposed for parameter estimation of the analytical model for a bridge isolated with a friction isolation bearing, and its efficiency in seismic fragility prediction was reported [49]. A machine learning method was proposed for the seismic response prediction of a bridge isolated with a two-stage friction pendulum bearing, and a user interface was developed for engineers for innovative isolator designs that are difficult to find in commercial design software [50]. A physics-informed neural network was proposed for inelastic strain prediction, and it was reported to have the potential to provide accurate predictions against tested earthquake scenarios for structural response prediction [51].

The analyses to be conducted within the scope of this study are, respectively, period analysis, re-centering analysis, and shear force analysis. These analyses will be conducted based on the lower, nominal, and upper limit values of the isolators. In the study, a total of 1000 different isolators will be analyzed, and the isolators will be differentiated according to certain parameters. These parameters are, respectively: friction coefficient, axial load acting on the isolator, radius of the curvature, number of isolators, short-period design spectral acceleration coefficient for maximum credible earthquake (MCE), 1 s period design spectral acceleration coefficient for maximum credible earthquake (MCE), short-period design spectral acceleration coefficient for design-based earthquake (DBE), and 1 s period design spectral acceleration coefficient for design-based earthquake (DBE). Period analysis, shear force analysis, and re-centering analysis were performed according to the isolator properties in the generated data, according to TBEC2018 [32] regulation. As a result of the analyses, designs that comply with the limit values were classified as Functional, and data rows that do not comply with the limit conditions and calculations that prevent the operation of the isolator were classified as Non-Functional isolators. The features obtained from the analyses were compiled into a dataset, and machine learning models were developed to predict the situations where the FPS isolators failed or functioned properly, depending on the limiting conditions that could lead to damage or loss of function. The learning models used inputs for the FPS isolator's friction coefficient, radius of the curvature, mean dead and live loads acting on the structure, total number of isolators, earthquake levels according to the Turkish Earthquake Code, and spectral acceleration coefficients for short- and long-period structures. These models were used to predict whether the isolators would function without breaking or if they were damaged in a way that prevented them from functioning. By comparing the developed AI models, the AI model with the highest accuracy for predicting the situations that prevent the FPS isolators from functioning was determined. In the literature, there are studies on damage detection in isolators [52], hysteresis behavior estimation [48], detection of damping capacity reduction [46], and structural response estimations [50,51]. The subject of this study, isolator operability determination, addresses limiting conditions. In this study, predictions are made for the operability of isolators, and the functionality of the isolator is determined according to parameters such as different load conditions, number of isolators, radius of the curvature, friction coefficient, and design spectral acceleration. The development of a prediction model for operability determination of the FPS-type isolator, one of the most common steel-based isolators, is innovative and in line with the goal it aims to achieve compared to other studies on isolator systems in the literature.

2. Materials and Methods

2.1. Friction Pendulum System

Friction pendulum system (FPS) devices have a mechanism that operates by the movement of a friction slider on a curved surface between a top and bottom plate. Figure 1 shows an example of a structure with an FPS and a classic FPS device.

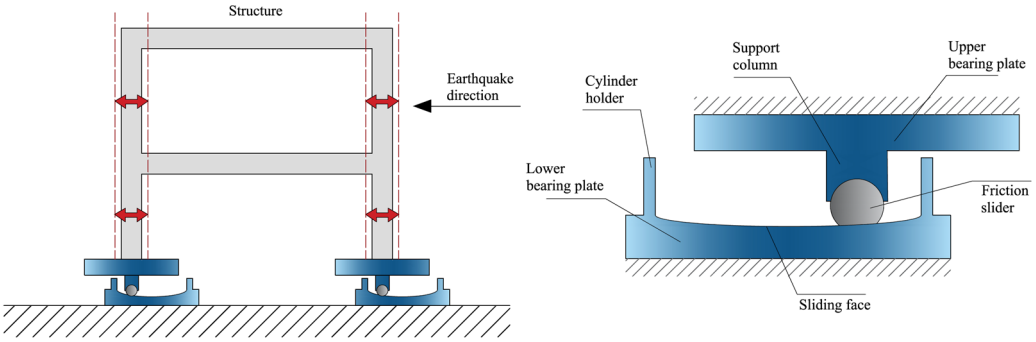


Figure 1. (**a**) FPS structure example, (**b**) FPS device.

The radius of curvature is effective in calculating the period of the FPS isolator. According to the 2018 Turkish Building Earthquake Code (TBEC2018) [32] (Equation (14.31)), the FPS period is calculated as in Equation (1). In the equation, the gravitational acceleration g is represented by the radius of curvature R_C. The equation [32] (Equation (14B.2)), which is included in the design of curved surface friction isolation units in TBEC 2018, states that the ratio of the vertical force to beyond the elasticity stiffness is equal to the radius of curvature. Furthermore, according to TBEC2018, it is stated that the isolator period should be less than or equal to 6 s for the maximum credible earthquake (MCE) [32] (Clause 14.3.7). Equation (1) has been revised according to this information and is in its final form.

$$T = 2\pi\sqrt{\frac{R_C}{g}} \leq 6s \tag{1}$$

For the MCE condition in TBEC2018 [32] (Clause 14.3.7), the difference between the internal forces of the isolation system at maximum displacement underground motion and those at half its maximum displacement must be 0.025 W or greater. Here, W is the total weight carried by the isolation system. In the isolation system, there are two main variables that affect the lateral (internal) force at maximum displacement. One is the friction force and the other is the pendulum effect. The friction force is equal to the product of the friction coefficient and the vertical force ($\boldsymbol{\mu_e W}$). The pendulum effect is calculated by dividing the maximum displacement in an MCE earthquake by the curvature radius and multiplying it by the vertical force $\left(\frac{D_M}{R_C}\boldsymbol{W}\right)$. In line with the effects that create internal forces, the limitation describing the clause in TBEC2018 [32] (Clause 14.3.7) is shown in Equation (2). $\boldsymbol{D_M}$, shown in Equation (2), represents the horizontal displacement, and $\boldsymbol{\mu_e}$ represents the friction coefficient.

$$\left(\mu_e W + \frac{D_M}{R_C}W\right) - \left(\mu_e W + 0.5\left(\frac{D_M}{R_C}W\right)\right) \geq 0.025W \tag{2}$$

The building's effective period for the MCE earthquake level of the building with the isolation system is shown in $\boldsymbol{T_M}$ as Equation (3), according to TBEC2018 [32] (Equation (14.31)), and the building effect period calculation for the DBE earthquake level is shown in $\boldsymbol{T_D}$ as Equation (4), according to TBEC2018 [32] (Equation (14.29)). $\boldsymbol{K_M}$ and $\boldsymbol{K_D}$ in the equations are the post-yield stiffness and effective stiffness values, respectively.

$$T_M = 2\pi\sqrt{\frac{W}{gK_M}} \tag{3}$$

$$T_D = 2\pi\sqrt{\frac{W}{gK_D}} \tag{4}$$

The effective stiffness value in a given loading cycle is symbolized by k_e. The K_M and K_D values are obtained by multiplying the effective stiffness by the number of isolators, according to TBEC2018 [32]. Equation (5) [32] (Equation (14B.3)) calculates k_e, and Equation (6) provides the equation used to calculate K_M and K_D. The total weight (W) carried by the isolation system is shown in Equation (7). The vertical force (P) calculation is shown in Equation (8). In these equations, N represents the number of isolators, F represents the maximum horizontal force in the loading cycle, P represents the vertical force, D represents the maximum displacement, G represents the dead load, and Q represents the live load.

$$k_e = \frac{F}{D} = \frac{P}{R_C} + \frac{\mu_e P}{D} \tag{5}$$

$$K_M,\ K_D = k_e \times N \tag{6}$$

$$W = P \times N \tag{7}$$

$$P = G + 0.3Q \tag{8}$$

The elastic spectral acceleration (S_{ae}) value is calculated based on the interval within which the structure's natural period lies. At MCE and DBE earthquake levels, it is calculated by substituting the building's effective period, T_M or T_D, for the structure's natural period. S_{ae} is calculated based on the range compatibility of the building period with the horizontal design spectrum corner periods, T_A and T_B. Equations (9)–(12) show the S_{ae} calculation for four intervals according to TBEC2018 [32] (Equation (2.2)). T_A and T_B periods are calculated as in Equations (13) and (14), respectively [32] (Equation (2.3)).

$$S_{ae}(T) = \left(0.4 + 0.6\frac{T}{T_A}\right)S_{DS} \qquad (0 \le T \le T_A) \tag{9}$$

$$S_{ae}(T) = S_{DS} \qquad (T_A \le T \le T_B) \tag{10}$$

$$S_{ae}(T) = \frac{S_{D1}}{T} \qquad (T_B \le T \le T_L) \tag{11}$$

$$S_{ae}(T) = \frac{S_{D1}T_L}{T^2} \qquad (T_L \le T) \tag{12}$$

$$T_A = 0.2\frac{S_{D1}}{S_{DS}} \tag{13}$$

$$T_B = \frac{S_{D1}}{S_{DS}} \tag{14}$$

S_{DS} in the equations indicates the design spectral acceleration coefficient for the short period, S_{D1} indicates the design spectral acceleration coefficient for the 1 s period, and T_L indicates the period defined for the transition to the constant displacement region in the horizontal elastic design spectrum. T_L is taken as 6 s [32] (Clause 2.3.4.1).

According to TBEC2018, the calculation of the horizontal displacement (D_M) of the isolation device considered for the MCE earthquake level is shown in Equation (15) [32] (Equation (14.30)). The index "M" is used for the MCE earthquake level, and the index "D" is used for the DBE earthquake level. According to TBEC2018, the displacement (D_D) calculation for the DBE earthquake level is calculated by replacing the expressions with the index "M" in Equation (16) [32] (Equation (14.28)) with the index "D". S_{ae}^{MCE} denotes the elastic spectral acceleration obtained by using T_M, which is the effective building period for the MCE earthquake level, instead of T in the calculations between Equations (9) and (12),

and S_{ae}^{DBE} denotes the elastic spectral acceleration obtained by using T_D in these equations for the DBE earthquake level. η_M and η_D in the equation denote the damping scaling coefficient for the MCE and DBE earthquake levels, respectively.

$$D_M = 1.3\left(\frac{g}{4\pi^2}\right)T_M^2\eta_M S_{ae}^{MCE} \tag{15}$$

$$D_D = 1.3\left(\frac{g}{4\pi^2}\right)T_D^2\eta_D S_{ae}^{DBE} \tag{16}$$

The effective damping ratio (β_e) is a parameter related to the friction coefficient, radius of curvature, and displacement. The calculation of the effective damping ratio, according to TBEC2018 [32] (Equation (14B.4)), is shown in Equation (17). Here, the calculation is made by taking the displacement value D_M for the MCE earthquake level and D_D for the DBE earthquake level instead of D, which represents the displacement. The effective damping ratio percentage (ξ) is calculated as in Equation (18).

$$\beta_e = \frac{2}{\pi}\left[\frac{\mu_e}{\mu_e + D/R_C}\right] \tag{17}$$

$$\xi = \beta_e \times 100 \tag{18}$$

The damping scaling coefficient (η) calculation is shown in Equation (19) [32] (Equation (14.32)). The damping scaling factors η_M for the MCE earthquake level and η_D for the DBE earthquake level use the ξ_M and ξ_D values calculated based on β_e, respectively.

$$\eta = \sqrt{\frac{10}{5+\xi}} \tag{19}$$

According to TBEC2018, the force calculation affecting the superstructure is given in Equation (20) [32] (Equation (14.36)) for the MCE earthquake level and in Equation (21) [32] (Equation (14.35)) for the DBE earthquake level. In the equations, the earthquake load reduction coefficient is denoted by "R".

$$V_M = \frac{S_{ae}^{MCE}(T_M)W\eta_M}{R} \tag{20}$$

$$V_D = \frac{S_{ae}^{DBE}(T_D)W\eta_D}{R} \tag{21}$$

When determining the nominal values of parameters in isolation systems, they are multiplied by specific coefficients. These values are the λ_{upper} and λ_{lower} coefficients. The formulas for calculating the λ_{upper} and λ_{lower} coefficients are shown in Equation (22) [32] (Equation (14.9)) and Equation (23) [32] (Equation (14.10)), respectively. The λ_{ae} values in the equations represent the multiplier to be used as a result of aging and environmental effects. The λ_{exp} multiplier is used for the effects of loading speed and heating, and the λ_{spect} multiplier is used for the effects of production-related changes.

$$\lambda_{upper} = \left[1 + 0.75\left(\lambda_{ae,upper} - 1\right)\right]\lambda_{exp,upper}\lambda_{spect,upper} \tag{22}$$

$$\lambda_{lower} = [1 - 0.75(1 - \lambda_{ae,lower})]\lambda_{exp,lower}\lambda_{spect,lower} \tag{23}$$

The λ_{ae}, λ_{exp}, and λ_{spect} values for friction surface isolation units are taken from the values table in TBEC2018 [32] (Table 14.3). Table 1 shows the multipliers used for friction pendulum isolation devices.

Table 1. Lower and upper limit recommended values for curved surface friction isolation systems.

λ	μ	
	Lower	**Upper**
λ_{ae}	1.00	1.20
λ_{exp}	0.70	1.30
λ_{spect}	0.85	1.15

It should be noted that the seismic responses of the FPS devices were obtained using analytical formulations defined in TBEC 2018 rather than through nonlinear dynamic finite element time–history analyses. The adopted approach aims to evaluate code-level operability limits of FPS isolators efficiently for large parametric datasets. While the response spectrum method cannot explicitly capture the full nonlinear seismic response, the nonlinear behavior of FPS devices is incorporated through friction-dependent effective stiffness, damping ratios, and displacement-based limit checks defined in TBEC 2018, which are widely accepted for design-level assessment of seismic isolation systems.

2.2. Machine Learning

Machine learning is an artificial intelligence technique developed to equip a machine with capabilities such as problem-solving, analysis, and other capabilities that mimic human abilities. The basic idea is to train a machine by initially showing it a portion of a dataset and then expecting it to predict the value closest to the expected result for a new data row. In machine training, the data attributes used as independent variables are called input, and the dependent variables to be predicted are called output. The machine divides the data into two groups, training and testing, and establishes a relationship between the data attributes and the outputs on the data allocated for training. Subsequently, output predictions in the dataset allocated for testing are calculated based on the relationship previously established by the machine between the input and output, and the model's success is determined by comparing its accuracy with the actual values in the data. Machine learning methods include supervised, semi-supervised, unsupervised, and reinforcement learning. Reinforcement learning involves learning through a trial-and-error process using a system of awards and punishments. The fundamental difference between other types of machine learning lies in the known details about the inputs used in data training. This study employs supervised learning. Some information about the supervised learning algorithms employed in this study is briefly summarized below.

Bagging classifier: Developed by Breiman [53], it is one of the ensemble learning algorithms. It divides the data into multiple subsets, collects the predictions of each subset, and performs classification based on the majority vote of these predictions. It stands out for its performance in handling complexity and overfitting in datasets [54].

Decision Tree Classifier: Decision Trees are a machine learning algorithm that divides data into small pieces, forming a tree-like structure. The inputs in the data represent the nodes of the tree, and the prediction results of the data segments allocated for testing represent the branches of the tree [55]. If the branches created are sufficiently discriminative for prediction, a decision is made about the class.

Random Forest Classifier: An ensemble learning algorithm developed by Breiman [56] that creates Decision Trees. The predictions of the trees created in the forest are collected, and majority voting is performed for the final prediction [57]. The applied algorithm framework is effective in preventing the overfitting of the model, increasing generalization ability, and reducing variance [57,58].

CatBoost Classifier: It is one of the ensemble learning algorithms aimed at gradient boosting [59,60]. It operates on the principle of strengthening weak learners in machine

learning and is quite effective in categorizing data. Its ability to process categorical data stems from the approach of replacing data labels with their mean values [60,61].

LightGBM Classifier: An ensemble learning algorithm developed by combining gradient boosting with data sampling and classification [62]. The LightGBM classifier has the ability to combine different features into a single feature, and LightGBM models optimize algorithm hyperparameters such as the number of gradient-boosted trees, maximum tree depth, and the learning rate for base learners [63].

XGBoost Classifier: An ensemble learning algorithm developed by Chen [64] based on gradient boosting, known as an extreme gradient boosting algorithm. It features automatic feature selection and increased convergence speed with boosted trees [65]. Each new tree attempts to reduce previous misclassifications.

2.3. Performance Metrics

Various metrics are used to evaluate the performance of machine learning models. Performance metrics vary depending on whether the problem is a regression or classification. This study evaluates a classification problem. For evaluating the artificial intelligence models on their prediction of classification types, model metrics such as accuracy, precision, recall, and the f1-score are used. These metrics are related to the degree to which predictions are correct or incorrect compared to the actual values. Table 2 provides the calculation equations for classification metrics.

Table 2. Performance metrics formulas for classification [66].

Metric	Formula
Accuracy	$\frac{TN+TP}{TN+TP+FN+FP}$
Precision	$\frac{TP}{TP+FP}$
Recall	$\frac{TP}{TP+FN}$
F1-Score	$\frac{2\times Precision\times Recall}{Precision+Recall}$

The letters N and P in the formulas in the table represent the negative and positive classes, respectively. The symbols T and F indicate correct and incorrect predictions, respectively. For example, TN indicates how many negative classes the model correctly predicted, and FP indicates how many positive classes the model incorrectly predicted. Based on these values, the classification metrics of accuracy, precision, recall, and F1-score are calculated.

In classification problems, a confusion matrix is formed based on the model's correct and incorrect predictions. This matrix is simply a breakdown of correct and incorrect predictions. Table 3 shows an example of a confusion matrix.

Table 3. Confusion matrix example [66].

		Actual	
		Class 1	**Class 2**
Prediction	**Class 1**	TP	FP
	Class 2	FN	TN

2.4. Model Evaluation

In validation of a machine learning model, it is important to evaluate how the model divides the data into training and testing sets. In this study, the K-fold cross-validation technique developed by Geisser and Eddy [67] was used, where the data is divided into k

parts for model validation. In the K-fold cross-validation method, the data is divided into k parts, with 1 part used for testing and the remaining parts used for training. Each of these k parts is then used in turn, with 1 part for testing and the remaining parts for training, yielding k results. The final performance is obtained by averaging the metrics obtained from the k validations. Figure 2 presents a visual summary of the 5-fold cross-validation method as an example.



Figure 2. The 5-fold cross-validation process.

In the machine learning framework, the generated dataset was first checked for completeness and consistency, and no missing values or outliers were identified in the dataset. All input features were used in their original physical units, and no feature scaling or normalization was applied, as the employed tree-based ensemble classifiers were inherently scale-independent. The dataset was randomly divided into training and holdout subsets using stratification, the model robustness was evaluated using stratified K-fold cross-validation (k = 10) on the training set, and the final evaluation was made on the holdout set (to prevent data leakage in the evaluation process). Stratified k-fold cross-validation was employed to preserve class distributions across folds, which is particularly important for imbalanced datasets. To ensure reproducibility and avoid overfitting, default hyperparameter settings in the Scikit-Learn package were adopted, and the performance of the models was assessed using multiple classification metrics including accuracy.

3. Numerical Example

In this study, period analysis, re-centering analysis, and shear force analysis were performed according to the maximum credible earthquake (MCE) and design-based earthquake (DBE) levels to prepare a dataset using friction pendulum system (FPS) isolators. Subsequently, based on the analysis results obtained, the data were organized for cases where the isolator operated without damage and cases where it failed by not meeting the boundary conditions. The dataset is based on 19 real structural design cases. For each design parameter, the minimum and maximum values observed in these cases were used to define admissible ranges. Additional data were generated by sampling within these bounds. All generated designs were evaluated against relevant regulations and isolator usability criteria, and each case was classified according to whether the isolator satisfied the code-based operability conditions. No explicit parameter correlations were imposed during data generation. Results were recorded whether the FPS isolator operated according to the isolator type and earthquake level, and this information was added to the data. Using the final dataset, a two-class machine learning model was developed to predict cases where the isolator operated and cases where it failed and lost its function. The input data for the model included the curvature radius of the FPS-type isolator, the friction coefficient, the total load acting on the structure, the total number of isolators, and the spectral acceleration coefficients obtained for short- and 1 s period structures at MCE and DBE earthquake

levels. The constants used in the period, re-centering, and shear force analyses are shown in Table 4.

Table 4. Design constants.

Symbol	Description	Value Range
μ_e	Friction coefficient	0.03–0.06
$G + 0.3Q$	Mean dead and live load	3452–8683 kN
R_C	Curvature radius	3–10 m
N	Total number of isolators	126–980
S_{DS}^{MCE}	Design spectral acceleration coefficient at short periods for MCE	1.232–4.420
S_{D1}^{MCE}	1 s period design spectral acceleration coefficient for MCE	0.308–2.230
S_{DS}^{DBE}	Design spectral acceleration coefficient at short periods for DBE	0.643–2.640
S_{D1}^{DBE}	1 s period design spectral acceleration coefficient for DBE	0.169–1.210
λ_{upper}	Multiplier used in lower limit calculations	0.60
λ_{lower}	Multiplier used in upper limit calculations	1.72
R	Response modification factor	1.0
V/W	The ratio of horizontal earthquake force to building weight	>0.15

The total average fixed and moving load, total number of isolators, MCE and DBE seismic levels, and spectral acceleration coefficients for short and 1 s period structures in the table have been selected from existing projects, and the friction coefficient and curvature radius values have been selected based on the values in the product catalogs. Period, re-centering, and shear force analyses were performed with attention to the selected value ranges in Table 4, and a 1000-row dataset was created for the prediction model. In classifying the dataset, cases where the isolator could function at MCE and DBE earthquake levels were designated as the "Functional" class, and cases where it could not perform its function based on the analyses were designated as the "Non-Functional" class. Ten rows from the dataset are shown in Table 5. There are 671 Functional and 329 Non-Functional classes in the dataset.

Table 5. Ten rows of the dataset.

FC	P	RC	N	SpA	Class
0.030	8618	3.0	326	0.9727	Functional
0.045	5565	6.9	152	1.8400	Functional
0.030	4442	5.5	126	1.1245	Functional
0.060	5758	8.1	150	2.6250	Non-Functional
0.044	7620	6.5	210	1.3122	Functional
0.034	6785	6.7	281	1.3478	Functional
0.051	4859	9.0	368	1.0215	Non-Functional
0.054	4646	7.1	889	1.7662	Functional
0.043	6069	8.5	920	0.9073	Non-Functional
0.047	5245	8.3	462	0.9805	Non-Functional

Table 5 shows the friction coefficient, FC; the average dead and live load, P; the radius of the curvature, RC; and the total number of isolators, N. Four columns were created, consisting of the short-period design spectral acceleration coefficient and the 1 s design spectral acceleration coefficient values for the MCE and DBE earthquake levels. Due to the high correlation between the spectral acceleration coefficient columns, a new data input column was created from the average of these four values for use in the machine learning model. Table 5 expresses the average values of the short-period and 1 s design

spectral acceleration coefficients for the MCE and DBE earthquake levels, calculated and shown in the SpA column. In the machine learning dataset, the four spectral acceleration coefficients corresponding to short- and long-period ranges at DBE and MCE levels were combined into a single representative spectral acceleration parameter (SpA). This choice was motivated by the high multicollinearity observed among these coefficients, as they are derived from the same regional seismic hazard definition and exhibit consistent scaling behavior. Averaging the coefficients reduces redundancy in the input space and improves the numerical stability of the learning models while preserving the overall intensity level of seismic demand relevant to isolator operability. It is acknowledged that this approach may mask period-specific spectral effects; however, given the classification-oriented objective of the study, the adopted simplification represents a practical balance between model simplicity and physical interpretability.

Statistical properties of the dataset are given in Table 6. The correlation matrix showing the relationship between the independent variables in the data is given in Figure 3.

Table 6. Statistical properties of the dataset.

Feature	FC	P	RC	N	SpA
	-	kN	m	-	-
Minimum variable	0.030	3452.00	3.00	126	0.588
Maximum variable	0.060	8683.00	10.00	980	2.625
Mean	0.045	6042.46	7.70	552	1.515
Standard deviation	0.009	1507.56	0.78	245.28	0.492
25%	0.037	4757.25	7.10	343.75	1.075
50%	0.045	5994.00	7.70	541.50	1.515
75%	0.053	7368.75	8.30	762.25	1.918



Figure 3. Correlation matrix.

Machine Learning Model

Within the scope of this study, prediction models were developed to determine whether friction pendulum system (FPS) isolators, to be used in various structures for maximum credible earthquake (MCE) and design-based earthquake (DBE) levels, function without damage, according to different isolator parameters. In machine learning models, six different ensemble learning algorithms were tested, and the algorithm that detected the isolator operating status with the highest accuracy was selected. The 10-fold cross-

validation technique was used in the training of the models. The data was split with 70% and 30% ratios; models were trained using 70% of the data, and the generalization performance of the models was tested using the remaining 30% of the dataset as the holdout set. The classification metrics (as the average of 10-folds) for training and test datasets derived from 70% of the data are shown in Table 7. In addition, the table also presents the metrics for the holdout set for each of the evaluated models.

Table 7. Performance metrics of learning models that predict the working status of the FPS isolation device.

		Decision Tree	XGBoost	Random Forest	LightGBM	CatBoost	Bagging
Precision	Train	1.0000	1.0000	1.0000	1.0000	0.9998	0.9964
	Test	0.9301	0.9536	0.9492	0.9534	0.9600	0.9381
	Holdout	0.9467	0.9467	0.9569	0.9597	0.9569	0.9621
Recall	Train	1.0000	1.0000	1.0000	1.0000	0.9999	0.9957
	Test	0.9233	0.9416	0.9416	0.9416	0.9481	0.9374
	Holdout	0.9396	0.9396	0.9446	0.9420	0.9446	0.9471
F1-score	Train	1.0000	1.0000	1.0000	1.0000	0.9998	0.9960
	Test	0.9253	0.9460	0.9445	0.9459	0.9525	0.9367
	Holdout	0.9430	0.9430	0.9504	0.9501	0.9504	0.9540
Accuracy	Train	1.0000	1.0000	1.0000	1.0000	0.9998	0.9965
	Test	0.9343	0.9529	0.9514	0.9529	0.9586	0.9443
	Holdout	0.9500	0.9500	0.9567	0.9567	0.9567	0.9600

Table 7 presents the models and evaluation metrics developed to predict the operability of the FPS-type isolator. Six different ML models were developed using the Bagging, Decision Tree, LightGBM, CatBoost, XGBoost, and Random Forest algorithms in the Scikit-Learn package [68]. All models were trained with the default hyperparameter values. The training set contained 700 records, and the models were trained to predict the operability of the FPS isolators (i.e., target variable) based on FC, P, N, RC, and SpA (i.e., input variables). During the training phase, a 10-fold CV strategy was implemented, and the 700 rows of data were divided into 10 folds: 9 folds were used for training and 1 fold was reserved for testing. This process has been repeated 10 times. In the total process, each fold served as the test data once, and the remaining folds served as training data in predicting the operability of the isolator. The performance metrics obtained from the 10 cycles were averaged and are presented in Table 7. Finaly, to test and ensure the generalizability of the model's performance, a holdout dataset of 300 rows, which the model has never seen before, was fed into to the machine learning model to evaluate the model's prediction ability on unseen data. The obtained results from this final dataset are included in Table 7 as holdout metrics.

4. Discussion

In this study, models were developed to predict the undisturbed operating condition of friction pendulum system (FPS) devices for various load conditions and FPS isolator parameters when designed for two different earthquake levels, according to the Türkiye Building Earthquake Code. To compare the performance of the models, a separate dataset that the machine had not seen before was tested, and the test success levels of the model, referred to as the holdout, were recorded. Figure 4 shows the holdout accuracy performance the machine learning models produced.

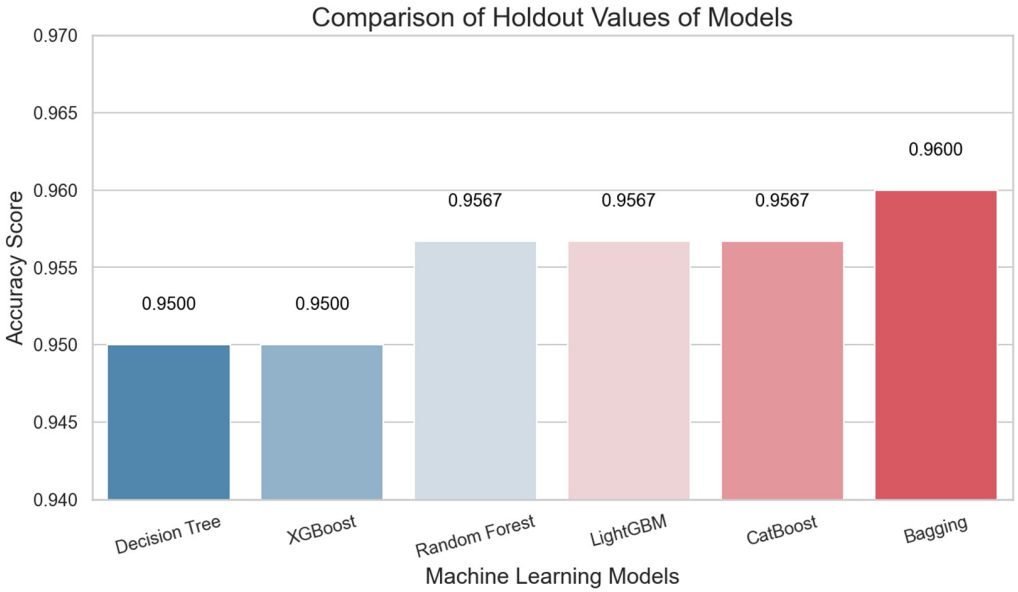


Figure 4. Comparison of holdout accuracy values of models.

When examining the graph provided in Figure 4, it can be seen that the accuracy of the models developed with ensemble learning algorithms was 95%. The highest holdout accuracy score was obtained from the Bagging model at 96.00%. After the Bagging model, the closest results were obtained by the Random Forest, LightGBM, and CatBoost models, all with the same accuracy (95.67%).

Decision Tree and XGBoost models are the two models showing the lowest performance (accuracy 95.00%). These two models, which had the same accuracy values, yielded only 1% lower accuracy than the highest-performing model. The Decision Tree classifier performs classification using a tree-like structure. It divides the data into branches of the tree according to features, and these branches are further divided internally. A leaf node is formed when the stopping criterion for branchingis met. The leaf node is the node where branching ends and the model makes its prediction. The XGBoost classifier is an algorithm that creates sequential trees and reduces overfitting through regularization. Each new tree is designed to correct the errors of the previous one in turn. When the last tree is reached, the final prediction is obtained; the model's prediction is a weighted sum of the outputs of all the trees. The reason these two algorithms yield the same accuracy result may be due to the easily distinguishable nature of the problem. The two classes in data are not present in equal amounts, leading to data imbalance. Despite this data imbalance, achieving a high accuracy score of 95% suggests that the Decision Tree and XGBoost models are related to their tree structure. The Decision Tree model produces a single tree, while XGBoost produces ordered trees. However, despite the ordered trees, the XGBoost model yielded the same result as the Decision Tree. In this situation, it can be concluded that a single tree is sufficient for model creation based on this dataset. In the XGBoost model, even though errors are corrected in each new tree, a single tree was sufficient for good performance, and the importance of other trees decreased. Random Forest, LightGBM, and CatBoost models yielded the closest results to the Bagging model, which had the highest score with the same accuracy (95.67%). The CatBoost model attempts to strengthen weak learning models and is known for its performance on categorical data. The Random Forest model generates independent, random trees and determines classes based on the majority vote of the tree outputs. The Random Forest classifier selects random features instead of all features when creating trees. Since all trees consist of different features, similarities in the trees are reduced, and the generalization ability of the model is increased. The LightGBM

classifier creates sequential trees. The main characteristic of the trees is that the next tree is generated to correct the errors of the previous tree, ensuring accurate prediction. The basis of these three models is that they are tree-based. Random Forest differs from the LightGBM and CatBoost models, which generate ordered trees through random feature selection and tree independence. LightGBM and CatBoost contribute to correcting the errors in the previous trees by generating ordered trees. The dataset consists of 1000 rows. The size of the dataset may have resulted in sufficient success with a single tree. However, these three models remain overly powerful, because a single tree is sufficient to achieve adequate performance for the dataset. The Bagging classifier divides the data into subsets, sums the predictions of each subset, and determines the class based on the majority vote of predictions. Since the subsets into which it divides the data directly affect the classifier's success, if a subset contains a small number of classes, it can become difficult for the machine to predict that class. In this way, the unbalanced distribution of classes affects the model's success. However, despite the imbalance in the data, the Bagging model achieved the highest performance in the results. The main reasons why the Bagging model achieved the highest score without being affected by class imbalance can be attributed to the small number of data features and their distinctiveness. This made it easier for the machine to acquire the ability to distinguish between classes. Furthermore, the accuracy difference between the training and holdout sets in the model is below 5%. This value indicates that the model does not suffer from overfitting. In other words, the Bagging model can predict classes using a simple tree structure with a small number of discriminating features.

Random Forest and Bagging models generate multiple independent Decision Trees for classification. Figure 5 shows an example of a tree generated by the Random Forest model, while Figure 6 shows the best Decision Tree extracted, generated by the Bagging model, which yields the highest accuracy.

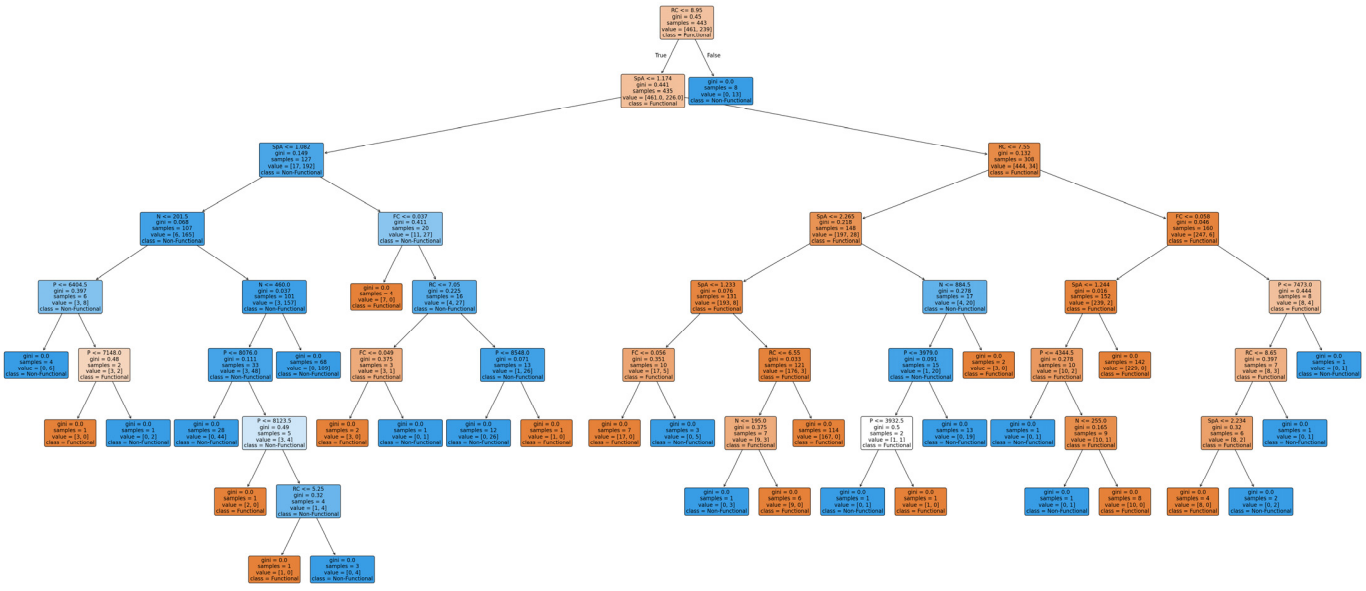


Figure 5. A representative Decision Tree extracted from the Random Forest model.

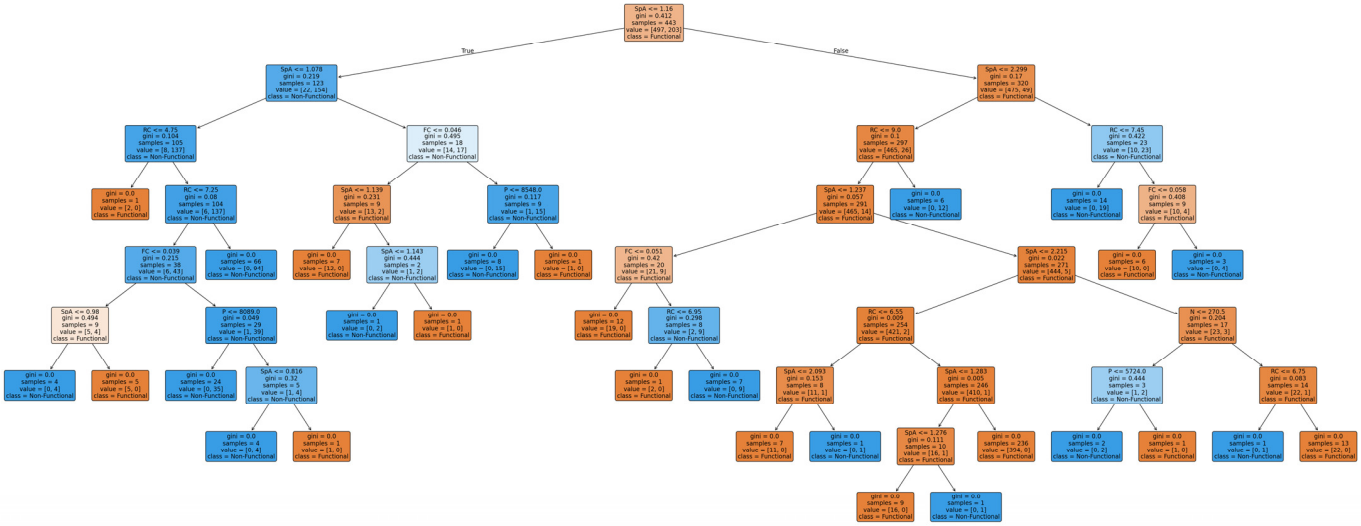


Figure 6. A representative best Decision Tree extracted from the Bagging model.

In this study, models were developed to identify situations where FPS-type isolators cannot function at MCE and DBE earthquake levels. Accuracy values indicate how accurately the model predicts all estimates. To enable a more precise comparison when evaluating the models, a Receiver Operating Characteristic (ROC) curve is plotted and Area Under the Curve (AUC) values are calculated. The ROC curve is plotted based on the relationship between the true positive rate (TPR) and the false positive rate (FPR). Here, the positive cases we are referring to and want to measure are those where the isolator has failed. In this study, the "Non-Functional" class in the dataset is used as positive for the ROC curve. The Non-Functional class represents situations where the isolator fails to function under the conditions of FPS device parameters and earthquake levels. Figure 7 shows the ROC curve plotted for all models.

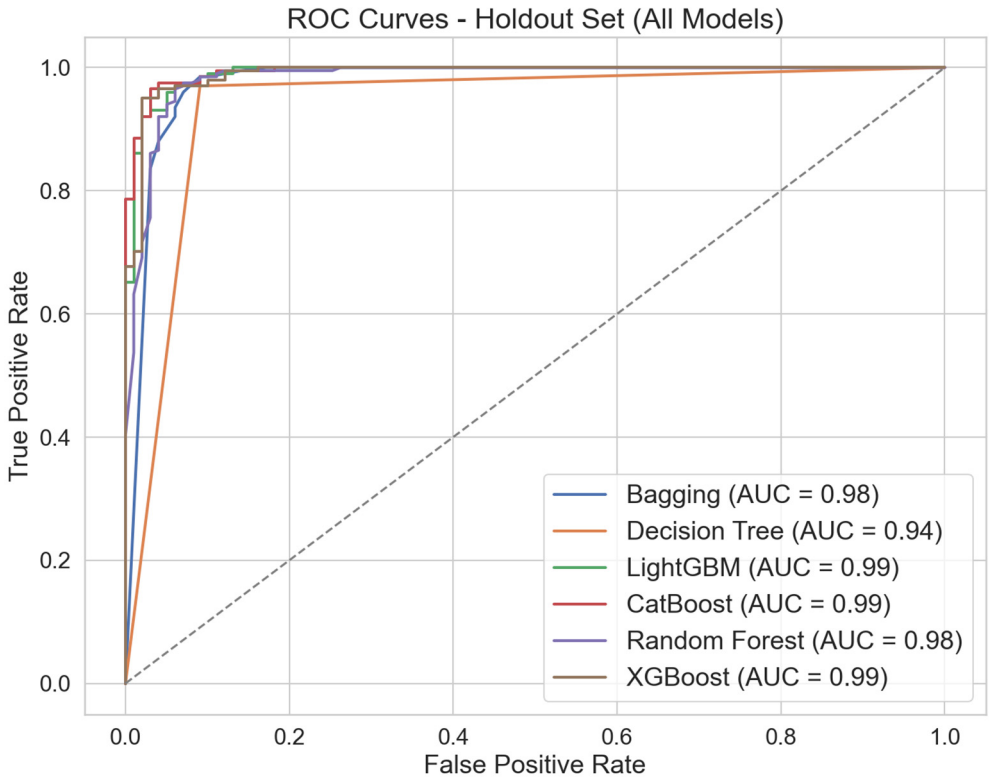


Figure 7. ROC curves for all models.

Looking at the legend in Figure 7, the AUC values of the curve can be seen. AUC values represent the area under the ROC curve. AUC values symbolize the model's ability to distinguish between classes. According to the calculated AUC values in the figure, the models that best distinguish between classes are the CatBoost, XGBoost, and LightGBM models with 0.99. The Bagging and Random Forest models achieved a value of 0.98, very close to the best three models. The accuracy value of the CatBoost model was very close to that of the Random Forest and XGBoost. In terms of the AUC value, the CatBoost, XGBoost, and LightGBM models were slightly ahead, by about 1%, of all models. In terms of precision, recall, and F1-score values, the best model was the Bagging model. Considering all performance metrics, it can be seen that the Bagging model gave more balanced results. CatBoost, XGBoost, and LightGBM achieved a very high AUC value. AUC values show that these models can distinguish between positive and negative classes with a high performance at all thresholds. One reason for this high performance may be that the data is a classification problem consisting of two classes.

The results have demonstrated that classification models achieved near-perfect accuracy on the training set, which indicates that models fit the training data extremely well. In fact, when test set accuracies are examined, the accuracies observed as being lower ranged between 0.93 and 0.96. This indicates a slight tendency to memorize training instances for all evaluated models, which is significantly apparent in the Decision Tree, XGBoost, Random Forest, and LightGBM models. In fact, for all models, the holdout accuracies (for the unseen data) align very well with the test set accuracies, which supports the reliability of the validation procedure and suggests that the models retain acceptable generalization ability despite their tendency to memorize training instances.

The distribution of classes in the dataset is important for comparing the model's discriminatory ability. Within the holdout set allocated for testing the constructed model, the distribution of classes gives the data balance ratio. In this study, the balance ratios of the class distribution in the datasets allocated for training and holdout testing are given in Table 8.

Table 8. Imbalance ratios for the holdout and training sets.

Dataset	Functional	Non-Functional	Imbalance Ratio
Holdout Set	201	99	2.0435
Training Set	470	230	2.0303

According to Table 8, 201 of the 300 holdout data points are Functional, and 99 are Non-Functional. Of the 700 data points in the training set, 470 are Functional and 230 are Non-Functional. The imbalance ratio (IR) for the holdout set is approximately 2.04 and for the training set is approximately 2.03. In both sets, the Functional class is approximately twice as numerous. The data is imbalanced at a 2:1 ratio. When datasets are unbalanced, it is important to plot the precision–recall (PR) curve. The data used in this study consists of two classes. The Functional class contains 671 data points, and the Non-Functional class contains 329. A lack of data in the Non-Functional class can lead to data imbalance. The PR curve is based on precision and recall values. In other words, it represents a proportion of positive classes. It is preferred in cases where the minority class is positive, as in this study. Figure 8 shows the precision–recall curve for all models.

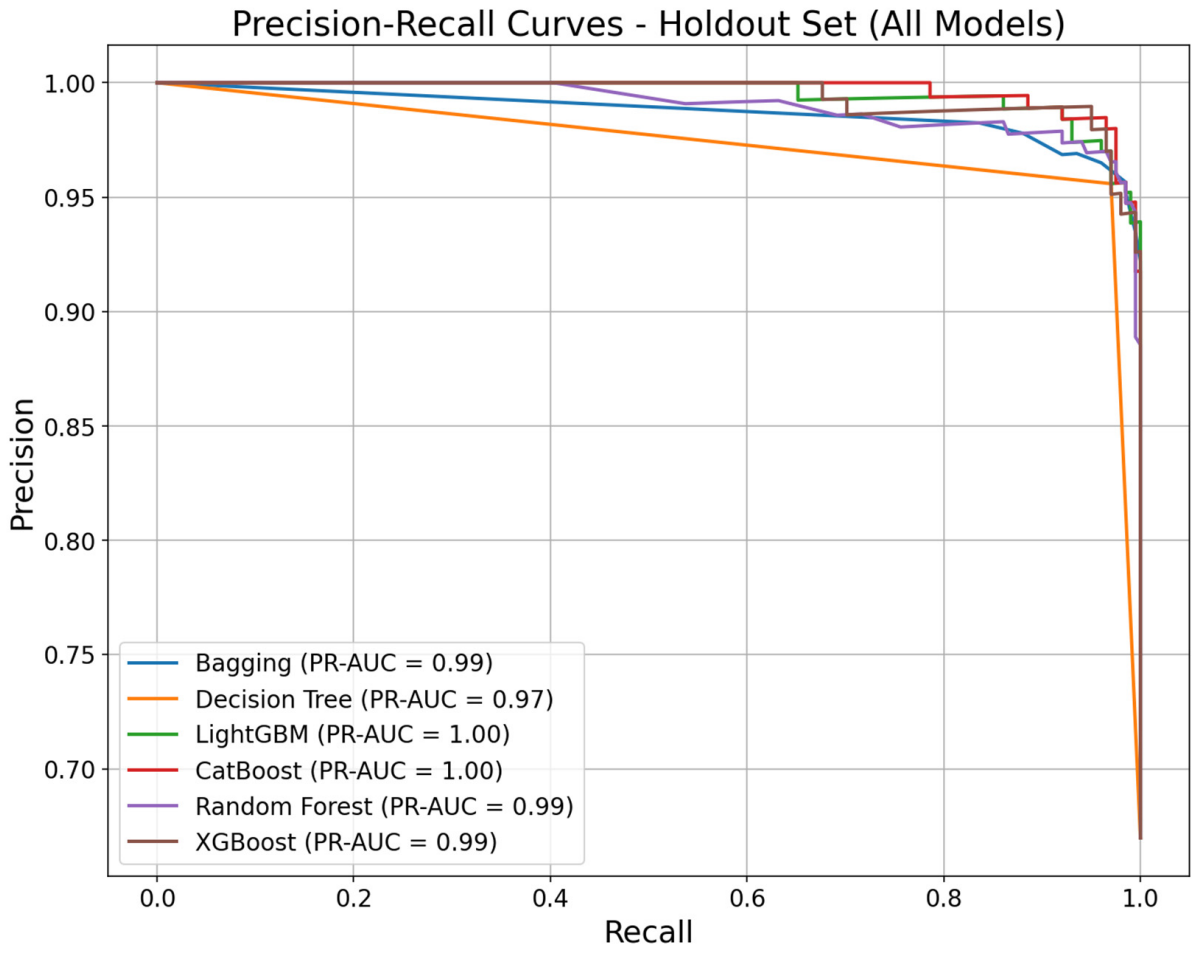


Figure 8. Precision–recall curves for all models.

Looking at the PR curve in Figure 8, it can be seen that the PR–AUC values are 0.97 and above. The highest score was achieved by the CatBoost and LightGBM models. The Random Forest, XGBoost, and Bagging models have the same values, with the CatBoost and LightGBM models having a higher AUC value by 1%. The XGBoost model achieved a PR–AUC value of 0.99 and also had the same high value on the ROC curve. However, overall, it lagged behind other models (Random Forest, LightGBM, CatBoost, and Bagging), according to classification metrics. The Decision Tree model showed the lowest performance, both according to classification metrics and the PR–ROC curve. The PR–AUC values of all models close to 1 indicate that the models have high class distinctiveness success and are effective at predicting the minority class, which is the positive class.

Confusion matrices showing the correct and incorrect predictions of the models in the dataset allocated for holdout are provided in Figure 9. In the figures, the class indicated as positive is the class indicating situations where FPStype isolator devices have malfunctioned and cannot operate (Non-Functional class).

In the confusion matrices shown in Figure 9, the number of incorrectly predicted positive classes (Non-Functional class) is lowest in the Bagging model. Only 99 of the 300 holdout data points are positively identified as the Non-Functional class. Errors were made in predicting the failure status of the FPS isolators in only 7 out of 99 cases. This corresponds to a misprediction rate of approximately 7% for isolator-unable-to-work situations. The next closest result was achieved by the CatBoost, Decision Tree, Random Forest, and XGBoost models, with nine incorrect predictions. So, four out of six models tested had the same error. The Random Forest and CatBoost models, with their high accuracy

and high AUC values on the ROC curve, incorrectly predicted 9 out of 99 values. The LightGBM model was the model that made the most errors (10 false) in predicting the minority group. The performance of the six models was approximately 90% successful in detecting isolator-unable-to-work situations. When looking at the distribution of data by class, the Non-Functional class is present in 329 rows of data and the Functional class in 671 rows. The ability to predict the Non-Functional class, a minority in the data, with an accuracy of approximately 90% demonstrates the successful overall performance of the models. These predicted values are scores obtained from the 30% of the data that the machine has never seen. When we look at the cases where the Functional class is misclassified in Figure 9, the LightGBM model ranks first as the model with the fewest errors, with three incorrect results, followed by the CatBoost and Random Forest models, with the same number of incorrect results (4). The Decision Tree and XGBoost models predicted the Functional class very similarly, with six falses. These false numbers represent the number of incorrectly predicted values out of 201 values. Of the CatBoost, LightGBM, and Random Forest models that made predictions with the lowest error rate, the LightGBM model predicted the Functional class with an approximately 1.5% error rate, while the CatBoost and Random Forest models had an approximately 2% error rate. The Bagging model that made the most errors in predicting the Functional class had an error rate of approximately 4%. Overall, all models predicted the Functional class fairly well, with an error rate not exceeding 4%.

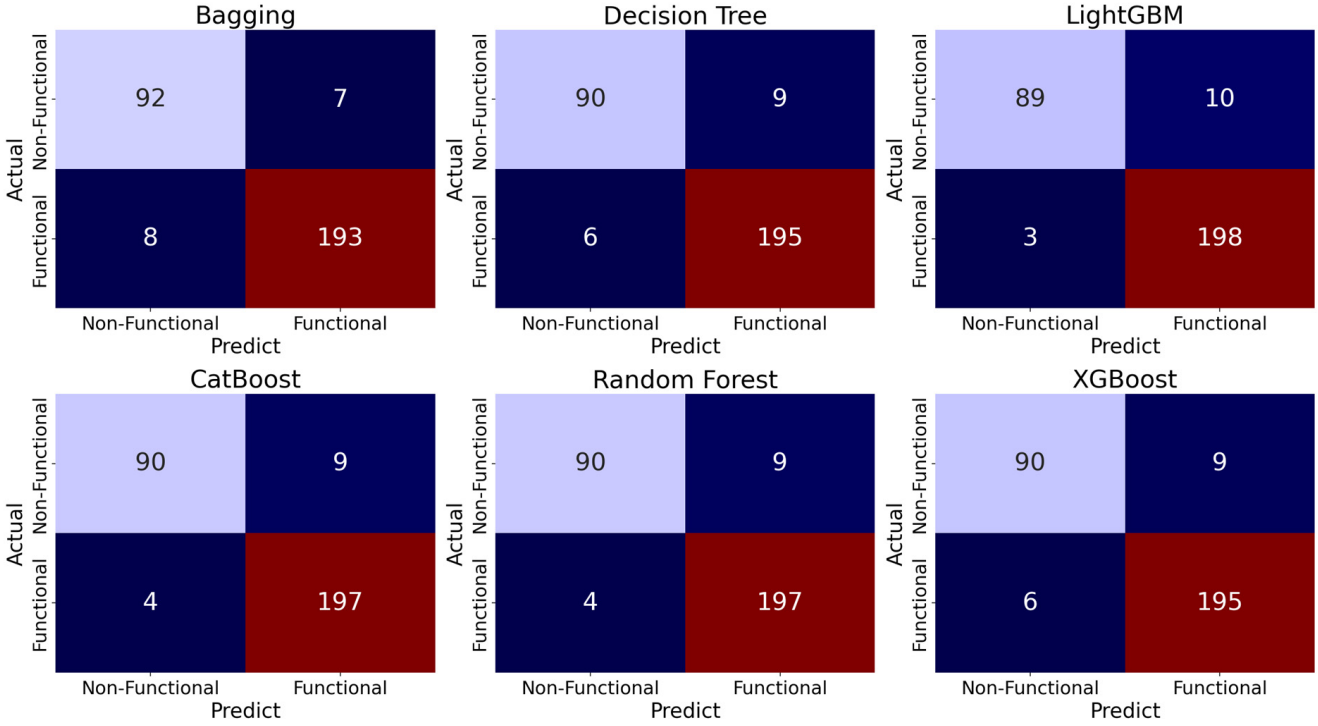


Figure 9. Confusion matrix for all models.

The CatBoost, XGBoost, and LightGBM models have an AUC of 0.99, indicating that they correctly predict almost all positive and negative classes. However, a clearer understanding requires an interpretation of the confusion matrix and holdout accuracy values. According to the holdout accuracy rates of the models in the test data, XGBoost has an accuracy rate of 95%, while LightGBM and CatBoost models have an accuracy rate of 95.67%. Additionally, the Random Forest and Bagging models yielded AUC values of 0.98. The holdout accuracies of these two models are 95.67% and 96%, respectively. Examining the confusion matrices, the Bagging model made the least errors in predicting minority

classes. It is evident that the AUC value alone should not be used to assess the accuracy of predictions. In conclusion, the Bagging model provides more balanced, robust, and reliable predictions.

Identifying effective features is crucial for the performance of a learning model. In this study, the Bagging model demonstrated the best predictive performance while also producing the least errors in identifying Non-Functional classes. In this study, the Bagging model demonstrated the best prediction performance. The second highest performance was shown by the XGBoost, LightGBM, and CatBoost models. Among these models, the LightGBM and CatBoost models outperformed the Random Forest model (AUC: 0.98, PR–AUC: 0.99), based on the AUC (0.99) and PR–AUC (1.00) values in the ROC curve. Although the LightGBM and CatBoost models have the same holdout accuracy, the CatBoost model outperformed the LightGBM model due to its lower error rate in both classification criteria and minority class prediction. LightGBM predicted the Functional class with the least errors among all models. Figure 10 shows the feature importance graph illustrating the effectiveness of the features used in the CatBoost model for classification. Figure 11 shows the importance graph of the effective features in the LightGBM model for classification.

An examination of Figure 10 reveals that the most influential feature for the CatBoost model is the mean design spectral acceleration coefficient at the MCE and DBE earthquake levels, denoted by SpA. This parameter is used to calculate the horizontal displacement of the isolator, which provides structural control, and the seismic force acting on the superstructure. It is expected to be an effective parameter in predicting the isolator's functionality. The relatively high effectiveness of approximately 60% in the CatBoost model indicates that the numerous trees generated by the model generate predictions based on the SpA feature and that it is a meaningful feature for the model. Input features are scanned for feature importance. When determining the most effective feature, the selection of decision points, called splits in the Decision Trees, is considered in the CatBoost models. The split selection is based on the reduction in the loss function. The effectiveness of the features used in the model in reducing the loss function indicates the importance of that feature in the model. In models that create ordered trees, such as CatBoost, the total loss reduction provided by the features collected from all trees determines the importance of the features in the model. The majority of the trees created according to the graph obtained from the CatBoost model used SpA in the decision nodes. Furthermore, the coefficient of friction (FC) and radius of the curvature (RC) significantly impacted the model's prediction performance, accounting for approximately 17% and 15%, respectively. The effects of dead and live loads (P) and the total number of isolators (N) affected the model by approximately 6% and 4%, respectively. Figure 11 shows that the SpA value is the most effective feature for classification in the LightGBM model, as well. However, the effectiveness of SpA in the LightGBM model is 20% less than in the CatBoost model. Furthermore, the effect of the total dead and live load and the total number of isolators is almost three-times as high as in the CatBoost model. Unlike CatBoost, the radius of curvature has a greater effect on classification than the friction coefficient for the LightGBM model.

A permutation feature importance graph is created to identify features that contribute to performance degradation. The dependence of a model's performance on these features is measured. In this measurement, the data is corrupted by shuffling the rows of the column whose effectiveness is to be measured based on the input features. In this way, the shuffled input column does not reflect its true value. After randomly shuffling the input rows, the model's performance is measured again. The loss in the newly measured performance is examined to determine the effectiveness of the shuffled data on model performance. Figure 12 shows the permutation feature importance graph for the holdout set of the Bagging model.

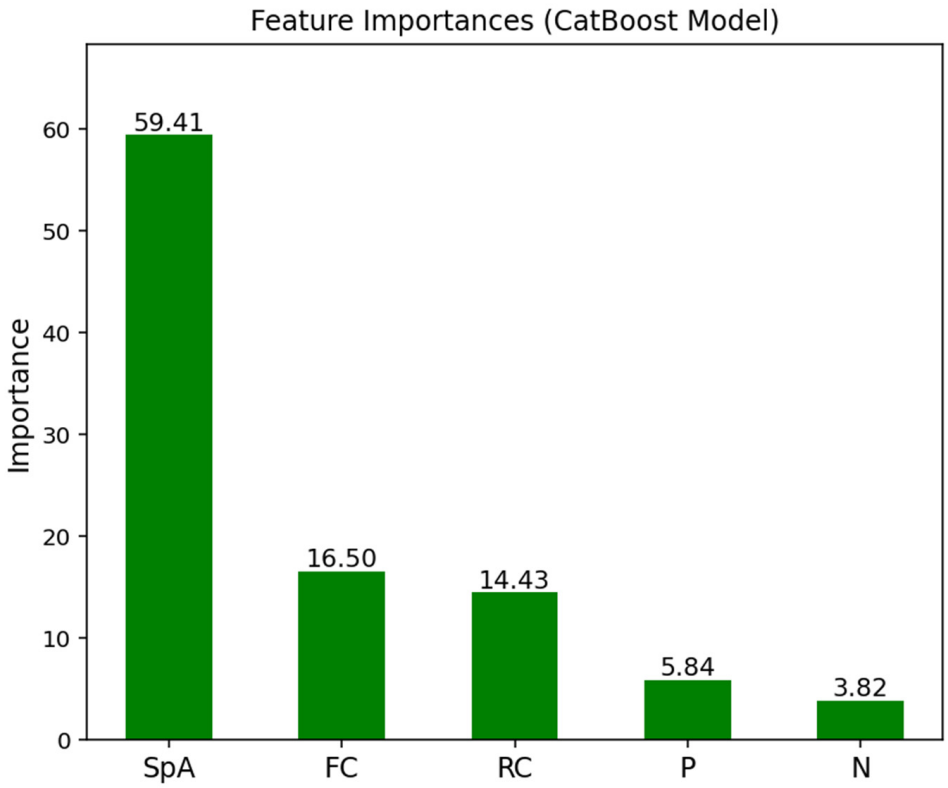


Figure 10. Feature importances graph for CatBoost Model.

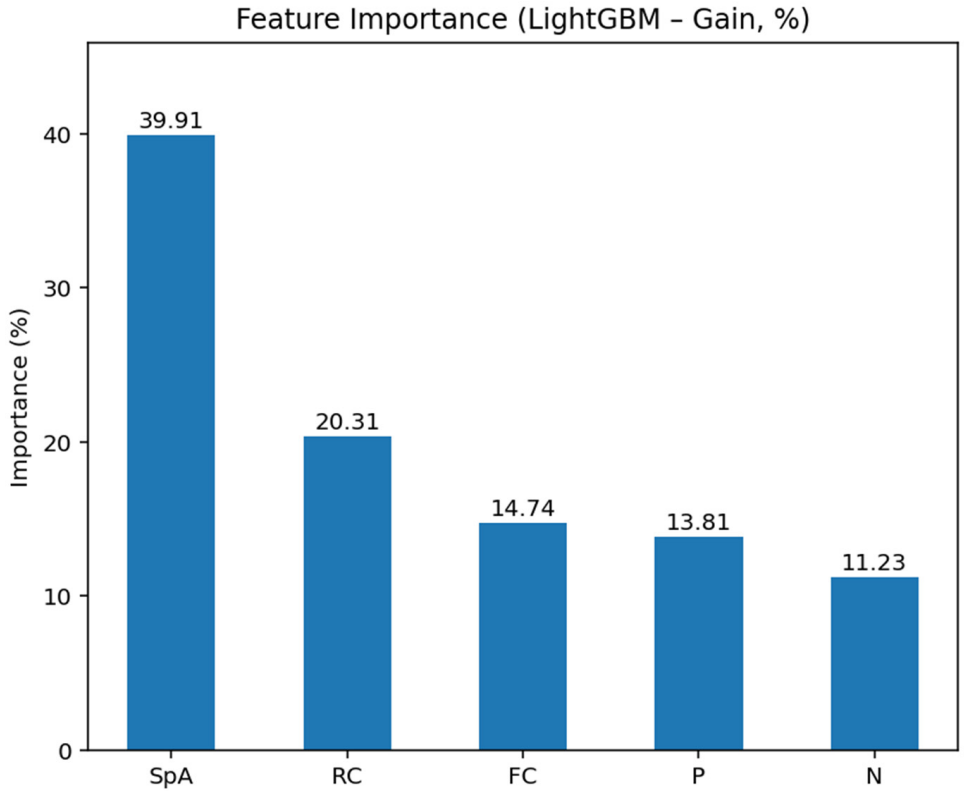


Figure 11. Feature importances graph for LightGBM Model.

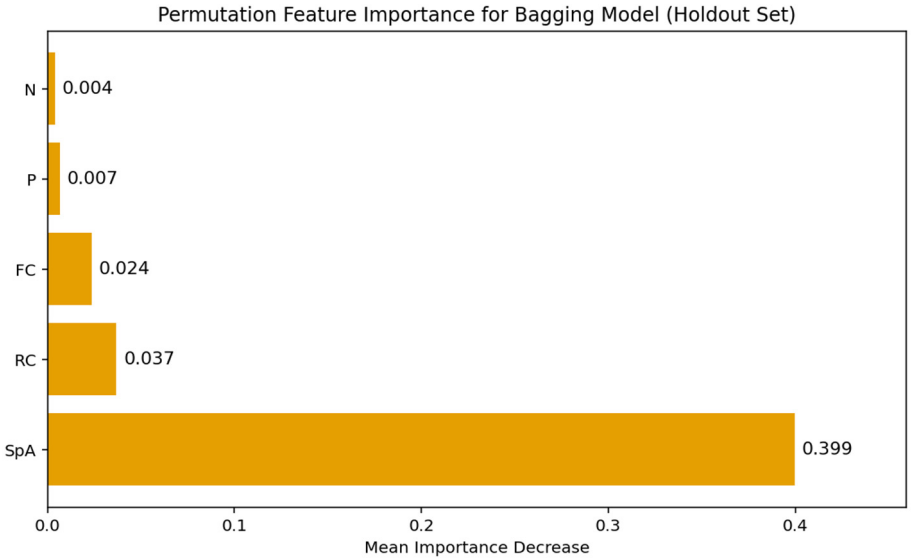


Figure 12. Permutation feature importance graph for Bagging model.

An examination of the graph in Figure 12 reveals that the feature that most significantly impacts model performance among the data inputs is the SpA column. SpA, also known as the mean design spectral acceleration coefficients, indicates that, when randomly shuffled rows do not reflect the actual values, the mean importance decrease in model performance significance is 0.399 units. Second in importance for performance is the radius of the curvature, followed by the friction coefficient. Because these values are design features that affect the isolator's control performance, their inclusion in the prediction model is significant.

When examining the importance graphs of the features affecting prediction models, it is observed that the design spectral acceleration coefficient (SpA) feature has the highest impact. The SpA feature affects the force acting on the superstructure under seismic loading. It directly affects the horizontal displacement of the isolators and the energy they expend to transfer this force to the superstructure. Therefore, it is expected that this feature has the highest importance for the prediction model. The radius of the curvature (RC) and friction coefficient (FC) properties of FPS-type isolators are among the main properties used by the isolator to dissipate seismic energy. The radius of the curvature property is effective in determining the period of FPS isolators. The magnitude of the radius of the curvature can increase the effective period and decrease the energy transferred to the superstructure. Due to its contribution to the period affecting the dynamic response of FPS isolators, it has become the second most important feature in model performance. Friction properties affect the horizontal movement of FPS isolators and therefore the amount of energy dissipation. A low coefficient of friction generally allows the isolator to move more freely horizontally. However, if this value is lower than necessary, it can lead to the uncontrolled movement of the isolator. Therefore, it is natural for it to affect the operability of FPS isolators. The radius of the curvature may have a slightly greater effect than the coefficient of friction due to its influence on the period. The other two properties used in the model are the p value, which represents the dead and live load, and the N value, which indicates the number of isolators. These properties are external factors independent of FPS isolators. Therefore, they are expected to be the least influential properties.

Among the models, the Bagging model has the highest holdout accuracy score. Furthermore, it stood out by making the fewest errors in predicting the minority class, the Non-Functional class. In the generated models, increases and decreases in data features have different effects on the model's orientation toward the Functional and Non-Functional

classes. SHapley Additive exPlanations (SHAP) analysis graphs are used to evaluate the effect of features on the model. This graph summarizes the effect of the features used in the prediction on the model outputs. The Shap analysis graph of the Bagging model is shown in Figure 13.

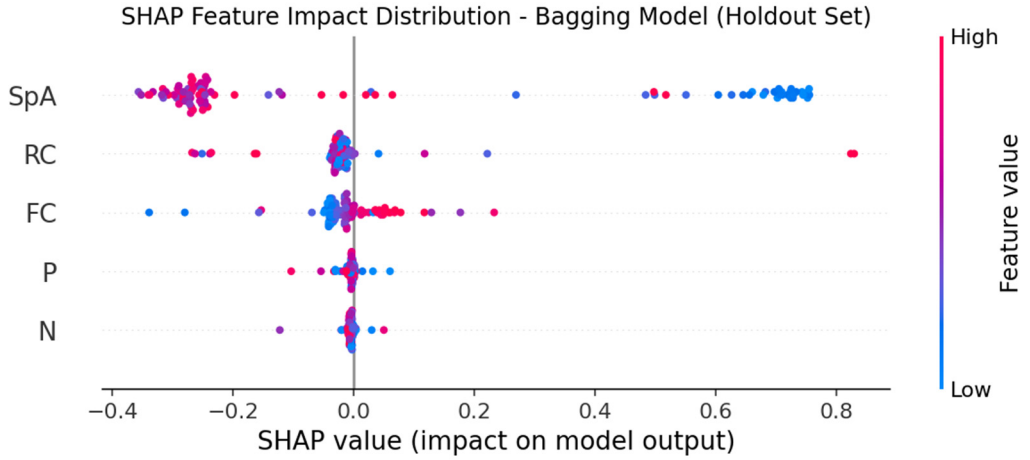


Figure 13. SHAP graph for Bagging model.

Examining the SHAP graph in Figure 13, it has to be seen that when the design spectral acceleration (SpA) feature is high, the model shifts its prediction probability towards the negative class, "Functional". As the SpA value decreases, the model class tends to predict the positive class, "Non-Functional". In the graph, the clustering for the SpA feature is on the left side, where the feature is high according to the color scale. This indicates that many data samples with high SpA tend to lean towards the negative class. Looking at the coefficient of friction (FC) feature, the model predicts the negative class when the FC value is low and the positive class when the FC value is high. This shows that FC is a consistent distinguishing feature. When the effect of the radius of the curvature (RC) property on the graph is examined, it is observed that high RC values generally tend to predict the Functional class, and rarely, some very high values show a tendency towards the Non-Functional class. Low RC values generally predict the Functional class. Furthermore, the graph reveals that low RC values rarely show a tendency towards the Non-Functional class. The clustering of RC values near the center indicates that there is no significant distinctive effect for centered RC values. The same applies to the coefficient of friction clustered near the center, load, and number of isolators. It is observed that a high number of isolators (N) generally leads the model to predict the Functional class, while for a low number of isolators, the tendency is scattered in the graph. In general, the effect of the change in the number of isolators on the model is limited horizontally. Furthermore, its clustering in the center indicates that, when the average is taken, it does not have a class-determining effect. Generally, it indicates that the number of isolators has a small effect on the model output. A similar situation applies to the p value, which represents the live and dead loads. According to the SHAP graph, these two features (N and P) have a small effect on the model output.

The proposed framework is based on code-defined analytical formulations and synthetic datasets, which enables the efficient evaluation of FPS isolator operability but also introduces certain limitations. Future studies should focus on validating the proposed machine learning models using experimental results and recorded earthquake ground motions, as well as incorporating nonlinear dynamic time–history analyses to better capture the transient response characteristics of isolated structures. In addition, extending the methodology to multi-stage and variable-curvature isolators, as well as to other seismic

isolation technologies such as lead–rubber bearings or sliding-type hybrid systems, would improve the generality and practical applicability of the approach.

5. Conclusions

In this study, machine learning models were developed to detect the performance and failure of FPS-type isolators under various earthquake spectral acceleration coefficients depending on the number of isolators, the friction coefficient, the radius of the curvature, and the conditions of fixed and moving loads. The proposed machine learning framework accurately identifies FPS isolator configurations that do not satisfy code-based operability criteria. More importantly, it functions as a rapid preliminary design and screening tool, enabling engineers to efficiently assess large combinations of isolator parameters for code compliance before conducting detailed analytical or numerical analyses. This capability reduces computational effort and design time while supporting informed early-stage decision-making in seismic isolation design.

The summary of the findings is as follows:

- CatBoost, LightGBM, and Random Forest models have been the most successful, with prediction accuracy rates 95.67%.
- Bagging model yielded the highest accuracy score, at 96%.
- The Bagging, Decision Tree, LightGBM, CatBoost, XGBoost, and Random Forest models used in the study yielded similar results according to all classification criteria, and the performance difference between the best chosen model, Bagging, and the others was at most 1%.
- The Bagging model predicted the minority class, i.e., Non-Functional isolators, with minimal error.
- The CatBoost model has demonstrated superior discrimination capabilities across all classes.
- Overall, all models predicted the Functional class fairly well, with an error rate not exceeding 4%. For the Non-Functional class, this rate was approximately 10%.
- Among the features used by CatBoost and LightGBM models for classification, the design spectral acceleration coefficient (SpA) value was the most influential on model performance (59.41% for CatBoost and 39.91% for XgBoost). Additionally, it was observed that the radius of the curvature and the coefficient of friction had a significant impact on the model's performance, ranging from approximately 15% to 20%.
- When the SpA feature, which has the highest impact in the Bagging model, is degraded, the model performance decreases by approximately 0.40 units.

Based on all of the findings, it was observed that machine learning models can predict the operational limitations of friction pendulum system (FPS) isolators under various isolator parameters and earthquake levels. It is anticipated that, in the future, with more comprehensive prediction models developed for isolator designs and the earthquakes they may be exposed to, artificial intelligence methods will accelerate the acquisition of preliminary information about isolator operational status after major earthquakes.

Author Contributions: Conceptualization, A.O., G.B. and Ü.I.; methodology, A.O., G.B. and Ü.I.; software, A.O., G.B., S.M.N. and Ü.I.; formal analysis, A.O. and B.K.; investigation, A.O. and B.K.; data curation, B.K. and A.O.; writing—original draft preparation, S.M.N., G.B., and A.O.; writing—reviewed and editing, G.B. and Z.W.G.; visulation S.M.N., G.B. and A.O.; supervision, G.B. and Z.W.G.; project administration, G.B. and Z.W.G. All authors have read and agreed to the published version of the manuscript.

Funding: This research received no external funding.

Institutional Review Board Statement: Not applicable.

Informed Consent Statement: Not applicable.

Data Availability Statement: The raw data supporting the conclusions of this article will be made available by the authors on request.

Conflicts of Interest: The authors declare no conflicts of interest.

References

1. Zayas, V.A.; Low, S.S.; Mahin, S.A. A simple pendulum technique for achieving seismic isolation. *Earthq. Spectra* **1990**, *6*, 317–333. [CrossRef]
2. Tsai, C.S.; Lin, Y.C.; Su, H.C. Characterization and modeling of multiple friction pendulum isolation system with numerous sliding interfaces. *Earthq. Eng. Struct. Dyn.* **2010**, *39*, 1463–1491. [CrossRef]
3. Moeindarbari, H.; Taghikhany, T. Seismic optimum design of triple friction pendulum bearing subjected to near-fault pulse-like ground motions. *Struct. Multidiscip. Optim.* **2014**, *50*, 701–716. [CrossRef]
4. Lee, D.; Constantinou, M.C. Quintuple friction pendulum isolator: Behavior, modeling, and validation. *Earthq. Spectra* **2016**, *32*, 1607–1626. [CrossRef]
5. Auad, G.; Almazán, J.L. Lateral Impact Resilient double concave Friction Pendulum (LIR-DCFP) bearing: Formulation, parametric study of the slider and three-dimensional numerical example. *Eng. Struct.* **2021**, *233*, 111892. [CrossRef]
6. Li, J.; Tan, P.; Yang, K.; Zheng, H.; Yamazaki, S.; Kishiki, S. Effect of bidirectional ground motion on the response of double concave friction pendulum systems. *Struct. Control Health Monit.* **2024**, *2024*, 1011161. [CrossRef]
7. Panchal, V.R.; Jangid, R.S. Variable friction pendulum system for seismic isolation of liquid storage tanks. *Nucl. Eng. Des.* **2008**, *238*, 1304–1315. [CrossRef]
8. Soni, D.P.; Mistry, B.B.; Jangid, R.S.; Panchal, V.R. Seismic response of the double variable frequency pendulum isolator. *Struct. Control Health Monit.* **2011**, *18*, 450–470. [CrossRef]
9. Namiranian, P.; Ghodrati Amiri, G.; Veismoradi, S. Near-fault seismic performance of triple variable friction pendulum bearing. *J. Vibroeng.* **2016**, *18*, 2293–2303. [CrossRef]
10. Shang, J.; Tan, P.; Zhang, Y.; Han, J.; Qin, J. Experimental and analytical investigation of variable friction pendulum isolator. *Eng. Struct.* **2021**, *243*, 112575. [CrossRef]
11. Yang, K.; Tan, P.; Shang, J.; Chen, H.; Li, J.; Xiang, Y.; Li, Y. Improved response spectrum analysis procedure for an adaptive variable friction pendulum isolated structure considering frictional dependency. *Soil Dyn. Earthq. Eng.* **2024**, *179*, 108549. [CrossRef]
12. Li, J.; Yang, K.; Xiang, Y.; Tan, P. Experimental investigation of frictional heating in variable friction pendulum bearings using thin-film thermocouples. *Tribol. Int.* **2025**, *212*, 110982. [CrossRef]
13. Tsai, C.S.; Chiang, T.C.; Chen, B.J. Finite element formulations and theoretical study for variable curvature friction pendulum system. *Eng. Struct.* **2003**, *25*, 1719–1730. [CrossRef]
14. Panchal, V.R.; Jangid, R.S. Seismic isolation of bridge using variable curvature friction pendulum system. In Proceedings of the 14th World Conference on Earthquake Engineering, Beijing, China, 12–17 October 2008.
15. Lu, L.Y.; Lee, T.Y.; Yeh, S.W. Theory and experimental study for sliding isolators with variable curvature. *Earthq. Eng. Struct. Dyn.* **2011**, *40*, 1609–1627. [CrossRef]
16. Shahbazi, P.; Taghikhany, T. Sensitivity analysis of variable curvature friction pendulum isolator under near-fault ground motions. *Smart Struct. Syst* **2017**, *20*, 23–33.
17. Lin, S.C.; Han, J.Q.; Zhao, H.T. Experimental and theoretical studies of bidirectional variable curvature friction pendulum bearing. *KSCE J. Civ. Eng.* **2020**, *24*, 1568–1580. [CrossRef]
18. Lin, S.C.; Wang, J.; Gao, S.; Zhao, H.T. Real-time hybrid test of a LNG storage tank with a variable curvature friction pendulum system. *Arch. Civ. Mech. Eng.* **2021**, *21*, 90. [CrossRef]
19. Wei, B.; Yang, Z.; Xiao, B.; Jiang, L.; Yu, Y. Simplified design theory of variable curvature friction pendulum bearing with adaptive capability and its application in railway bridge. *Structures* **2024**, *63*, 106370. [CrossRef]
20. Jangid, R.S. Optimum friction pendulum system for near-fault motions. *Eng. Struct.* **2005**, *27*, 349–359. [CrossRef]
21. Yin, G.; Ma, M.; Jia, P.; Ma, X. Parameter Optimization of Friction Pendulum Bearings Based on the Adaptive Genetic Algorithm Considering the Overall Evolutionary Status. *Buildings* **2024**, *14*, 435. [CrossRef]
22. Sharma, A.; Jangid, R.S. Performance of variable curvature sliding isolators in base-isolated benchmark building. *Struct. Des. Tall Spec. Build.* **2012**, *21*, 354–373. [CrossRef]
23. Duan, C. Parametric Analysis of Friction Pendulum System Inter-Story Isolation Structure Based on Benchmark Model. In Proceedings of the 2021 7th International Conference on Hydraulic and Civil Engineering & Smart Water Conservancy and Intelligent Disaster Reduction Forum (ICHCE & SWIDR), Nanjing, China, 6–8 November 2021; IEEE: Piscataway, NJ, USA, 2021; pp. 136–142.

24. Fu, T.; Wang, W.; Ge, N.; Wang, X.; Zhang, X. Intelligent computing and simulation in seismic mitigation efficiency analysis for the variable friction coefficient RFPS structure system. *Neural Comput. Appl.* **2021**, *33*, 925–935. [CrossRef]
25. Zhang, J.; Ding, Y.; Guan, X.; Ou, J. Mechanical properties of innovative prefabricated friction pendulum bearing with concrete-filled steel tube system. *J. Build. Eng.* **2023**, *69*, 106170. [CrossRef]
26. Zhuang, P.; Hu, X.; Yang, T.Y. Experimental and numerical studies on the seismic behavior of spherical reticulated shells with sliding isolation bearings. *Structures* **2024**, *70*, 107645. [CrossRef]
27. Castaldo, P.; Palazzo, B.; Della Vecchia, P. Seismic reliability of base-isolated structures with friction pendulum bearings. *Eng. Struct.* **2015**, *95*, 80–93. [CrossRef]
28. Li, J.; Kishiki, S.; Yamada, S.; Yamazaki, S.; Watanabe, A.; Terashima, M. Effect of Friction Dependencies on the Bidirectional Earthquake Response of Double Concave Friction Pendulum Bearings. *J. Earthq. Eng.* **2024**, *28*, 777–798. [CrossRef]
29. Xian, Z.; Tan, P.; Zheng, W.; Yang, K.; Xiang, Y.; Zheng, Y. Seismic performance of inter-story isolated structure with shape memory alloy variable curvature friction pendulum bearings. *Soil Dyn. Earthq. Eng.* **2026**, *200*, 109737. [CrossRef]
30. Cao, S.; Huang, J. Development and characterization of a gravity-well-based triple friction pendulum system. *Soil Dyn. Earthq. Eng.* **2025**, *197*, 109486. [CrossRef]
31. Deringöl, A.H.; Güneyisi, E.M. Effect of friction pendulum bearing properties on behaviour of buildings subjected to seismic loads. *Soil Dyn. Earthq. Eng.* **2019**, *125*, 105746. [CrossRef]
32. AKH Engineering. *Turkey Building Earthquake Code*; Republic of Turkey Ministry of Interior Disaster and Emergency Management Authority: Ankara, Turkey, 2018.
33. Çakat, G.; Alemdar, Z.F. Seismic base isolation of a typical hospital structure with a friction pendulum isolator. *J. Struct. Eng. Appl. Mech.* **2019**, *2*, 1–11. [CrossRef]
34. Kaatsız, K.; Alıcı, F.S.; Sucuoglu, H.; Tanışer, S.; Kale, Ö. Seismic performance assessment of base isolation systems in five hospitals during the M w 7.8 and M w 7.6 2023 earthquakes in Southeast Turkey. *Earthq. Spectra* **2025**, *41*, 176–197. [CrossRef]
35. Das, R.; Sharma, M.L.; Wason, H.R.; Choudhury, D.; Gonzalez, G. A seismic moment magnitude scale. *Bull. Seismol. Soc. Am.* **2019**, *109*, 1542–1555. [CrossRef]
36. Moeindarbari, H.; Taghikhany, T. Seismic reliability assessment of base-isolated structures using artificial neural network: Operation failure of sensitive equipment. *Earthq. Struct.* **2018**, *14*, 425.
37. Nakabayash, T.; Wada, K.; Utsumi, Y. Automatic detection of air bubbles with deep learning. In Proceedings of the 37th International Symposium on Automation and Robotics in Construction (ISARC), Kitakyushu, Japan, 27–29 October 2020; IAARC Publications: Oulu, Finland, 2020; pp. 1168–1175.
38. Barakat, S. Design of the base isolation system with artificial neural network models. In Proceedings of the 2020 4th International Conference on Compute and Data Analysis, Silicon Valley, CA, USA, 9–12 March 2020; pp. 79–83.
39. Al-Rawashdeh, M.; Yousef, I.; Al-Nawaiseh, M. Predicting the inelastic response of base isolated structures utilizing regression analysis and artificial neural network. *Civ. Eng. J.* **2022**, *8*, 1178–1193. [CrossRef]
40. Yavas, M.S.; Gao, Z.; Mekaoui, N.; Saito, T. A machine learning-based hybrid seismic analysis of a lead rubber bearing isolated building specimen. *Soil Dyn. Earthq. Eng.* **2023**, *174*, 108217. [CrossRef]
41. Gu, R.; Jia, J.; Bian, J.; Guo, T. Machine learning-based rapid damage states assessment and seismic response prediction of highway bridges supported by unbonded laminated rubber bearing. *Structures* **2025**, *75*, 108826. [CrossRef]
42. Nguyen, H.D.; Dao, N.D.; Shin, M. Machine learning-based prediction for maximum displacement of seismic isolation systems. *J. Build. Eng.* **2022**, *51*, 104251. [CrossRef]
43. Zhang, X.; Men, J.; Zhang, X.; Pu, Y. A machine learning method: Hybrid ANN-PSO model to predict LRB mechanical parameters. *Smart Constr.* **2025**, *2*, 0020. [CrossRef]
44. Zeng, Y.; Chen, T.; Xiong, F.; Deng, K.; Xu, Y. Combination of active sensing method and data-driven approach for rubber aging detection. *Struct. Health Monit.* **2024**, *23*, 2310–2322. [CrossRef]
45. Zeng, Y.; Deng, C.; Xiong, F.; Peng, H.; Xu, Y.; Liu, Y. DetachSense rubber bearing for convenient axial load prediction using active sensing and Bayesian-optimized deep neural network. *Eng. Struct.* **2024**, *315*, 118503. [CrossRef]
46. Ocak, A.; Işıkdag, Ü.; Bekdaş, G.; Nigdeli, S.M.; Kim, S.; Geem, Z. Prediction of damping capacity demand in seismic base isolators via machine learning. *CMES Comput. Model. Eng. Sci.* **2024**, *138*, 2899–2924. [CrossRef]
47. Habib, A.; Yildirim, U. Developing a physics-informed and physics-penalized neural network model for preliminary design of multi-stage friction pendulum bearings. *Eng. Appl. Artif. Intell.* **2022**, *113*, 104953. [CrossRef]
48. Mekaoui, N.; Hada, S.; Saito, T. Deep learning model for prediction of non-linear cyclic hysteresis of seismic isolation devices: Full-scale experimental validation. *Soil Dyn. Earthq. Eng.* **2023**, *169*, 107873. [CrossRef]
49. Zhu, Y.; Zhou, S.; Zhong, J.; Wang, H. AI-assisted analytical model of seismic displacement estimation for frictional isolated bridge portfolios under pulse-like ground motions. *Soil Dyn. Earthq. Eng.* **2024**, *187*, 108991. [CrossRef]
50. Akhlaq, H.; Peng, T.; Jitteh, K.; Khan, M.S. Machine Learning Models for Predicting Seismic Response of a Novel Two-Stage Friction Pendulum Isolated Bridge Structure. *IEEE Access* **2025**, *13*, 105165–105182. [CrossRef]

51. Habib, A.; Yildirim, U. Developing block-based physics-informed multi-layered neural network model for simulating the inelastic response of base-isolated structures. *Neural Comput. Appl.* **2025**, *37*, 8963–8986. [CrossRef]
52. Zhang, M.; Guo, T.; Zhu, R.; Zong, Y.; Liu, Z.; Xu, W. Damage identification of seismic-isolated structure based on CAE network using vibration monitoring data. *Eng. Struct.* **2023**, *283*, 115873. [CrossRef]
53. Breiman, L. Bagging predictors. *Mach. Learn.* **1996**, *24*, 123–140. [CrossRef]
54. Channamallu, S.S.; Almaskati, D.; Kermanshachi, S.; Pamidimukkala, A. Autonomous vehicle safety: An advanced bagging classifier technique for crash injury prediction. *Multimodal Transp.* **2025**, *4*, 100189. [CrossRef]
55. Morales, E.F.; Escalante, H.J. A brief introduction to supervised, unsupervised, and reinforcement learning. In *Biosignal Processing and Classification Using Computational Learning and Intelligence*; Academic Press: Cambridge, MA, USA, 2022; pp. 111–129.
56. Breiman, L. Random forests. *Mach. Learn.* **2001**, *45*, 5–32. [CrossRef]
57. Asif, R.; Upadhyay, D.; Zaman, M.; Sampalli, S. Enhancing Diabetes Risk Prediction: A Comparative Evaluation of Bagging, Boosting, and Ensemble Classifiers with SMOTE Oversampling. *Inform. Med. Unlocked* **2025**, *57*, 101661. [CrossRef]
58. Shahhosseini, M.; Hu, G.; Pham, H. Optimizing ensemble weights and hyperparameters of machine learning models for regression problems. *Mach. Learn. Appl.* **2022**, *7*, 100251. [CrossRef]
59. Developers, C. *CatBoost: High Performance Gradient Boosting on Decision Trees Library*; ascl-2108; Astrophysics Source Code Library (ASCL): Houghton, MI, USA, 2021.
60. Dorogush, A.V.; Ershov, V.; Gulin, A. CatBoost: Gradient boosting with categorical features support. *arXiv* **2018**, arXiv:1810.11363. [CrossRef]
61. Rahimi, M.; Karbasi, M.; Jamei, M.; Rezaverdinejad, V.; Malik, A.; Farooque, A.A.; Yaseen, Z.M. Meticulous estimation of maize actual evapotranspiration: A comprehensive explainable CatBoost algorithm reinforced with Jackknife uncertainty paradigm. *Comput. Electron. Agric.* **2025**, *237*, 110599. [CrossRef]
62. Ke, G.; Meng, Q.; Finley, T.; Wang, T.; Chen, W.; Ma, W.; Liu, T.Y. Lightgbm: A highly efficient gradient boosting decision tree. In Proceedings of the 31st International Conference on Neural Information Processing Systems (NeurIPS 2017), Long Beach, CA, USA, 4–9 December 2017; pp. 3146–3154.
63. Jain, P.; Yedukondalu, J.; Chhabra, H.; Chauhan, U.; Sharma, L.D. EEG-based detection of cognitive load using VMD and LightGBM classifier. *Int. J. Mach. Learn. Cybern.* **2024**, *15*, 4193–4210. [CrossRef]
64. Chen, T.; Guestrin, C. Xgboost: A scalable tree boosting system. In Proceedings of the 22nd ACM SIGKDD International Conference on Knowledge Discovery and Data Mining, San Francisco, CA, USA, 13–17 August 2016; pp. 785–794.
65. Tipu, R.K.; Panchal, V.R.; Pandya, K.S. Multi-objective optimized high-strength concrete mix design using a hybrid machine learning and metaheuristic algorithm. *Asian J. Civ. Eng.* **2023**, *24*, 849–867. [CrossRef]
66. Rainio, O.; Teuho, J.; Klén, R. Evaluation metrics and statistical tests for machine learning. *Sci. Rep.* **2024**, *14*, 6086. [CrossRef] [PubMed]
67. Geisser, S.; Eddy, W.F. A predictive approach to model selection. *J. Am. Stat. Assoc.* **1979**, *74*, 153–160. [CrossRef]
68. Pedregosa, F.; Varoquaux, G.; Gramfort, A.; Michel, V.; Thirion, B. Scikit-Learn: Machine Learning in Python. 2022. Available online: https://scikit-learn.org/stable/about.html#citing-scikit-learn (accessed on 1 November 2025).

Disclaimer/Publisher's Note: The statements, opinions and data contained in all publications are solely those of the individual author(s) and contributor(s) and not of MDPI and/or the editor(s). MDPI and/or the editor(s) disclaim responsibility for any injury to people or property resulting from any ideas, methods, instructions or products referred to in the content.